

Supramolecular control of the magnetic anisotropy in two-dimensional high-spin Fe arrays at a metal interface

Pietro Gambardella^{1,2,3*}, Sebastian Stepanow^{1,4}, Alexandre Dmitriev^{4,5}, Jan Honolka⁴, Frank M. F. de Groot⁶, Magalí Lingenfelder⁴, Subhra Sen Gupta⁷, D. D. Sarma⁷, Peter Bencok⁸, Stefan Stanescu⁸, Sylvain Clair³, Stéphane Pons³, Nian Lin⁴, Ari P. Seitsonen⁹, Harald Brune³, Johannes V. Barth¹⁰ and Klaus Kern^{3,4}

Magnetic atoms at surfaces are a rich model system for solid-state magnetic bits exhibiting either classical^{1,2} or quantum^{3,4} behaviour. Individual atoms, however, are difficult to arrange in regular patterns^{1–5}. Moreover, their magnetic properties are dominated by interaction with the substrate, which, as in the case of Kondo systems, often leads to a decrease or quench of their local magnetic moment^{6,7}. Here, we show that the supramolecular assembly of Fe and 1,4-benzenedicarboxylic acid molecules on a Cu surface results in ordered arrays of high-spin mononuclear Fe centres on a 1.5 nm square grid. Lateral coordination with the molecular ligands yields unsaturated yet stable coordination bonds, which enable chemical modification of the electronic and magnetic properties of the Fe atoms independently from the substrate. The easy magnetization direction of the Fe centres can be switched by oxygen adsorption, thus opening a way to control the magnetic anisotropy in supramolecular layers akin to that used in metallic thin films^{8–11}.

The control of magnetic anisotropy is a key issue in the development of molecule–metal interfaces for magnetic applications, both at the single-molecule¹² and extended-film level¹³. In metallic multilayers used as storage media or spin-valve devices at present, tuning of the magnetic anisotropy is achieved either by a careful choice of the overlayer/substrate composition and thickness or by oxidation of the magnetic elements^{11,14,15}. Recent studies showed that the magnetization direction of surface-supported paramagnetic molecules can be controlled through exchange coupling with a magnetic film, which provides robust ferromagnetic properties but does not enable each molecule to be switched independently from the substrate or its neighbours^{16,17}. Alternatively, theoretical work suggested that the sign of magnetic anisotropy could be reversed in metal–organic complexes by exploiting oxidation processes that affect the hybridization of molecular orbitals with metal states carrying non-zero orbital magnetization¹⁸.

Here, we investigate supramolecular self-assembly on a non-magnetic Cu surface as a means to produce two-dimensional

(2D) arrays of regularly spaced Fe spins, the magnitude and magnetic anisotropy of which are manipulated by lateral and axial molecular ligands. Although Fe atoms adsorbed on Cu(100) constitute a metallic system owing to the substantial overlap of the Fe 3*d* and 4*s* states with the Cu bands, and exhibit a Kondo temperature of about 55 K (ref. 7), X-ray absorption spectroscopy (XAS) and multiplet calculations shows that Fe–Cu hybridization is drastically weakened by square-planar coordination to 1,4-benzenedicarboxylate molecules (hereafter indicated as terephthalate acid or TPA), leading to a high-spin configuration with strongly localized Fe²⁺ character. X-ray magnetic circular dichroism (XMCD) measurements confirm the presence of sizeable spin moments at the Fe sites, together with a large orbital moment and in-plane magnetic anisotropy that originate from spin–orbit-induced mixing of ground and first excited molecular states. The Fe centres in the supramolecular arrays act as selective adsorption sites for O₂, which produces an out-of-plane reorientation of the easy magnetization axis at the Fe sites. Furthermore, the saturation of the orbital magnetic moments of TPA-coordinated Fe is found to be strongly anisotropic, revealing an unusual feature of surface-supported magnetic systems.

The co-deposition of transition-metal ions and organic ligands on crystalline surfaces offers the potential to design supramolecular grids with programmable structural and chemical features^{19,20}, where the interaction with the substrate is used to stabilize a planar geometry^{21,22}. Fe_x(TPA)_y complexes on Cu(100) constitute a prototypical 2D hetero-assembled system forming a variety of mono- and bi-nuclear network structures, in which the morphology is determined by the Fe:TPA stoichiometry, substrate symmetry and annealing temperature^{22–24}. Figure 1a shows a scanning tunnelling microscopy image of the square-symmetry array of self-assembled mononuclear Fe(TPA)₄ complexes investigated here. Each Fe atom is coordinated to four TPA molecules through Fe–carboxylate bonds, with the supramolecular Fe(TPA)₄ units organized in a (6 × 6) unit cell with respect to the underlying Cu lattice (Fig. 1c). Weak hydrogen-bonding interactions between

¹Centre d'Investigacions en Nanociència i Nanotecnologia (ICN-CSIC), UAB Campus, E-08193 Barcelona, Spain, ²Institució Catalana de Recerca i Estudis Avançats (ICREA), E-08010 Barcelona, Spain, ³Institut de Physique des Nanostructures, Ecole Polytechnique Fédérale de Lausanne (EPFL), CH-1015 Lausanne, Switzerland, ⁴Max-Planck-Institut für Festkörperforschung, D-70569 Stuttgart, Germany, ⁵Department of Applied Physics, Chalmers University of Technology, 41296 Göteborg, Sweden, ⁶Department of Chemistry, Utrecht University, 3584 CA Utrecht, The Netherlands, ⁷Solid State and Structural Chemistry Unit, Indian Institute of Science, Bangalore 560 012, India, ⁸European Synchrotron Radiation Facility, BP 200, F-38043 Grenoble, France, ⁹Institut de Minéralogie et de Physique des Milieux Condensés, Université Pierre et Marie Curie, F-75252 Paris, France, ¹⁰Physik-Department E20, Technische Universität München, D-85748 Garching, Germany. *e-mail: pietro.gambardella@icrea.es.

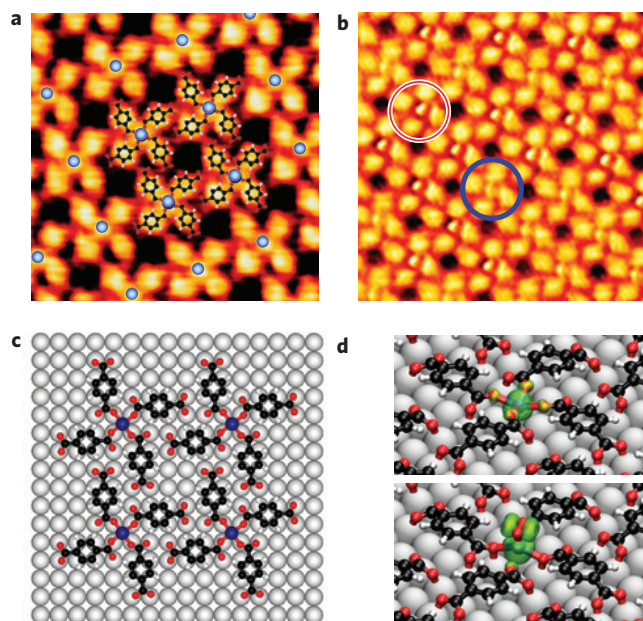


Figure 1 | Planar supramolecular layers of Fe-TPA complexes self-assembled on Cu(100). **a**, Fe(TPA)₄ array; blue dots indicate the position of Fe atoms. Each Fe centre is coordinated to four deprotonated oxygen ligands of the surrounding TPA molecules. STM image size 62 × 62 Å². **b**, Selective uptake of O₂ by Fe; a change of STM contrast is observed for O₂-Fe(TPA)₄ (red circle) at the Fe location compared with Fe(TPA)₄ (blue circle). Image size 84 × 84 Å². **c**, Top-view model of Fe(TPA)₄ coordination and supporting Cu(100) substrate. **d**, Relaxed Fe(TPA)₄ and O₂-Fe(TPA)₄ supramolecular structures obtained by DFT. Fe (blue), O (red), C (black) and H (white) atoms are shown together with the spin density distribution (green).

the complexes favour long-range order extending over entire terraces of the substrate²³ (see Supplementary Information, Fig. S1). The resultant superlattice of individual Fe centres has perfect 15 × 15 Å² periodicity. Despite the four-fold lateral coordination to the carboxylate ligands and the residual interaction with Cu, Fe centres are chemically active, forming an array of coordinatively unsaturated sites. On exposure to O₂, scanning tunnelling microscopy images indicate that selective adsorption of oxygen takes place close to Fe on-top positions, as demonstrated by the change of contrast in Fig. 1b. The structural properties of both Fe(TPA)₄ and O₂-Fe(TPA)₄ complexes as well as their interaction with the substrate were further characterized using density functional theory (DFT) calculations, as described in the Methods section. The relaxed supramolecular structures are shown in Fig. 1d together with an isocontour of the spin density distribution; the optimal O₂-Fe(TPA)₄ geometry corresponds to O₂ chemisorbed on Fe with the O–O axis parallel to the surface plane, in agreement with the angular dependence of the oxygen XAS (see Supplementary Information, Fig. S4).

L-edge X-ray absorption spectra provide a unique probe of the bonding and magnetic properties of transition-metal ions²⁵, with the extra advantage of extreme sensitivity to surface-dilute systems²⁶. This is of crucial importance for the present study, as the intensity, lineshape and polarization dependence of dipole-allowed $2p \rightarrow 3d$ transitions offer information on the spin state, oxidation state and ligand field of Fe ions in an element-selective way. Figure 2 shows the XAS and XMCD spectra of 0.025 monolayers of Fe deposited on Cu(100) at room temperature (Fig. 2a), equivalent to the Fe content in the supramolecular arrays, Fe(TPA)₄ (Fig. 2b) and O₂-Fe(TPA)₄ (Fig. 2c). The XAS intensity, shown after Cu background subtraction, was measured at 8 K with magnetic field

B = 6 T applied out-of-plane ($\theta = 0^\circ$) and at grazing incidence ($\theta = 70^\circ$) for parallel (I^+) and antiparallel (I^-) alignment of the photon helicity with **B**. More details about the measurements are given in Supplementary Information. The comparison of Fig. 2a–c reveals telltale differences in the XAS lineshape: whereas Fe/Cu(100) exhibits broad L_3 and L_2 peaks typical of a metal, pronounced narrowing of the spectral features and a well-defined multiplet fine structure is observed for the Fe-TPA complexes, similar to the spectra of Fe ions in bulk metal–organic compounds²⁷. These changes, related to ligand-induced modifications and localization of the Fe *d*-orbitals, indicate that true coordination bonds have been formed between the Fe centres and carboxylate ligands, with partial decoupling of Fe from the metal substrate. Interestingly, electron localization effects are found to be more pronounced in self-assembled Fe(TPA)₄ compared with chemically synthesized Fe–porphyrin molecules evaporated on metal films¹⁷. We find that the XAS (I^+ , I^-) and the XMCD ($I^+ - I^-$) spectral shape depend markedly on the orientation of the beam with respect to the molecular arrays. This is in essence a linear dichroism effect²⁵ related to the anisotropic spatial distribution of the Fe *d*-electrons in a low-symmetry environment that cannot be observed in bulk-like molecular powder studies²⁷, but is resolved here owing to the planar alignment of the complexes. Both the large XAS L_3/L_2 branching ratio and the strong XMCD intensity of Fe(TPA)₄ and O₂-Fe(TPA)₄ point towards a high-spin Fe configuration for the complexes, against the tendency of the Cu electrons to reduce the Fe moment through the Kondo interaction⁷.

To gain more insight into the electronic and magnetic properties of the Fe centres, we carried out XAS and XMCD simulations using ligand-field multiplet theory with the inclusion of charge-transfer effects²⁵. The molecular environment was modelled by a crystal-field potential defined by the parameters Dq , Ds and Dt , as appropriate for C_{4v} symmetry. Covalent mixing of the metal valence *d*-orbitals with the ligand *p*-orbitals was simulated using a valence bond configuration interaction scheme, whereby the ground state of Fe is taken to be a linear combination of $3d^n$ and $3d^{n+1} \underline{L}$ configurations, with \underline{L} indicating a ligand hole. We tested different combinations of d^5 , d^6 and d^7 configurations, corresponding to Fe³⁺, Fe²⁺ and Fe¹⁺, respectively. The simulations show that the ground state of Fe in both Fe(TPA)₄ and O₂-Fe(TPA)₄ complexes possesses almost pure d^6 character, with maximum 14% and 15% $d^7 \underline{L}$ weight, respectively, depending on the hopping parameters assumed in the calculations (see Supplementary Information, Table S1). Within this admixture range, the calculated spectra show only minor differences and are in very good agreement with the experimental data, as shown in Fig. 2d,e. This result has important consequences as (1) it proves that the Fe *d*-orbitals are interacting mainly with the ligands and only weakly perturbed by the metallic substrate (not so for the *s*-states, see Supplementary Information), (2) it shows that Fe(TPA)₄ and O₂-Fe(TPA)₄ constitute high-spin Fe²⁺ complexes, which are expected to exhibit zero-field splitting and anisotropic *g*-factors, that is, strong magnetic anisotropy properties in the language of molecular magnetism. In contrast, high-spin Fe³⁺, with a half-filled *d*-shell, would have only minor orbital contributions to the magnetization and very small magnetic anisotropy.

Consistently with the geometry of the O ligands, we find that the crystal-field splitting patterns (Fig. 3c,d) are close to square planar and square pyramidal for Fe(TPA)₄ and O₂-Fe(TPA)₄, respectively, whereas the strong tetragonal distortion that characterizes Fe(TPA)₄ reduces significantly in O₂-Fe(TPA)₄ owing to the presence of the apical ligand (see Supplementary Information, Table S1). DFT calculations further show that the total number of Fe valence electrons changes from 6.67 to 6.33 following O₂ chemisorption, but that the population of the $3d$ -states remains essentially stable (see Supplementary Information, Table S2), in

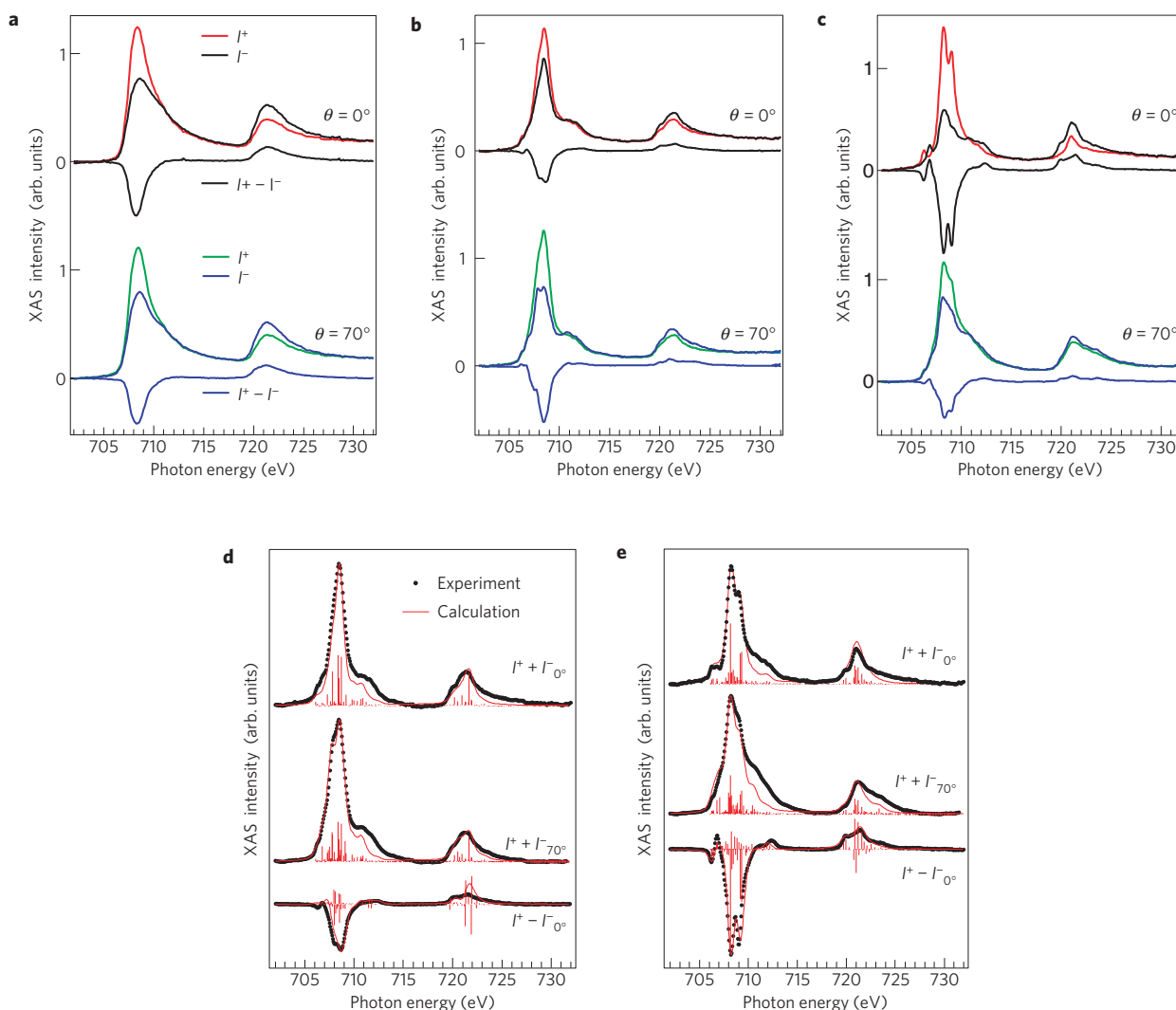


Figure 2 | Circularly polarized X-ray absorption spectra of $\text{Fe}(\text{TPA})_4$, $\text{O}_2\text{-Fe}(\text{TPA})_4$ and $\text{Fe}/\text{Cu}(100)$ measured at the $\text{Fe } L_{2,3}$ -edge and calculated multiplet structure. **a–c, XAS intensity of 0.025 monolayer $\text{Fe}/\text{Cu}(100)$ (**a**), $\text{Fe}(\text{TPA})_4$ (**b**) and $\text{O}_2\text{-Fe}(\text{TPA})_4$ (**c**) for parallel (I^+) and antiparallel (I^-) orientation of the photon helicity with field-induced magnetization. Spectra were recorded in the electron-yield mode at $T = 8 \text{ K}$ and $\mathbf{B} = 6 \text{ T}$ at normal ($\theta = 0^\circ$) and grazing incidence ($\theta = 70^\circ$). The XMCD signal ($I^+ - I^-$) is shown for each orientation. **d,e**, Calculated XAS and XMCD spectra of $\text{Fe}(\text{TPA})_4$ (**d**) and $\text{O}_2\text{-Fe}(\text{TPA})_4$ (**e**). See text for details.**

agreement with the ligand-field simulations. There are 0.8 excess electrons localized on the O_2 ligand, the largest fraction of which is supplied by the Cu substrate acting as a charge reservoir, a behaviour that is specific to surface-supported metal–organic systems. Notably, the formation of the supramolecular complexes is accompanied by a substantial increase of the Fe–substrate distance, calculated as 2.32 Å for individual Fe atoms on Cu(100), 2.71 Å in $\text{Fe}(\text{TPA})_4$ and 3.32 Å in $\text{O}_2\text{-Fe}(\text{TPA})_4$, showing together with XAS how the Fe–Cu metal interactions progressively weaken with increasing number of ligands. A more detailed discussion of the crystal-field and DFT electronic-structure results is reported in Supplementary Information.

Confirmation of the strong magnetic anisotropy behaviour of Fe in the supramolecular complexes was obtained by angle-dependent XMCD measurements, exploiting the XMCD proportionality to the projection of the Fe magnetic moment on the X-ray incidence direction. The relative magnitude of the XMCD spectra at $\theta = 0^\circ$ and 70° in Fig. 2 indicates that, whereas $\text{Fe}/\text{Cu}(100)$ has weak out-of-plane anisotropy, the $\text{Fe}(\text{TPA})_4$ easy axis lies in-plane. O_2 adsorption at the Fe sites, however, further drives an abrupt magnetic anisotropy reorientation transition, rotating the Fe easy

axis out-of-plane. The field dependence of the XMCD signal in Fig. 3a,b underlines the strong change in magnetic anisotropy induced by O_2 . This effect is comparable to that reported for ultrathin metal films^{9–11}, but opposite in sign with respect to oxygen-dosed Fe layers on Cu(100) (ref. 11). With respect to bulk molecular crystals, the planar and open coordination structure of the self-assembled Fe array makes such a system extremely sensitive to chemisorption, providing straightforward control of the preferred Fe spin orientation. Through the analysis of the XAS and XMCD spectra, we can further identify the cause for the easy-axis switch in the metal–organic complexes, revealing a different mechanism from the one proposed by Atodiresei and co-workers¹⁸ based on the control of the metal oxidation state. Our calculations show that only the ligand field is affected by O_2 adsorption, whereas the formal Fe oxidation does not change. As demonstrated by the crystal-field level schemes in Fig. 3c,d, the axial O_2 ligand induces a change of the Fe ground state from A_{1g} to E_g . This effect can be understood also in an intuitive way, as the on-top O_2 molecule binds axially to the d_{z^2} Fe orbital, thus effectively pushing up the antibonding A_{1g} state (that is, the term with d_{z^2} -like symmetry) relative to

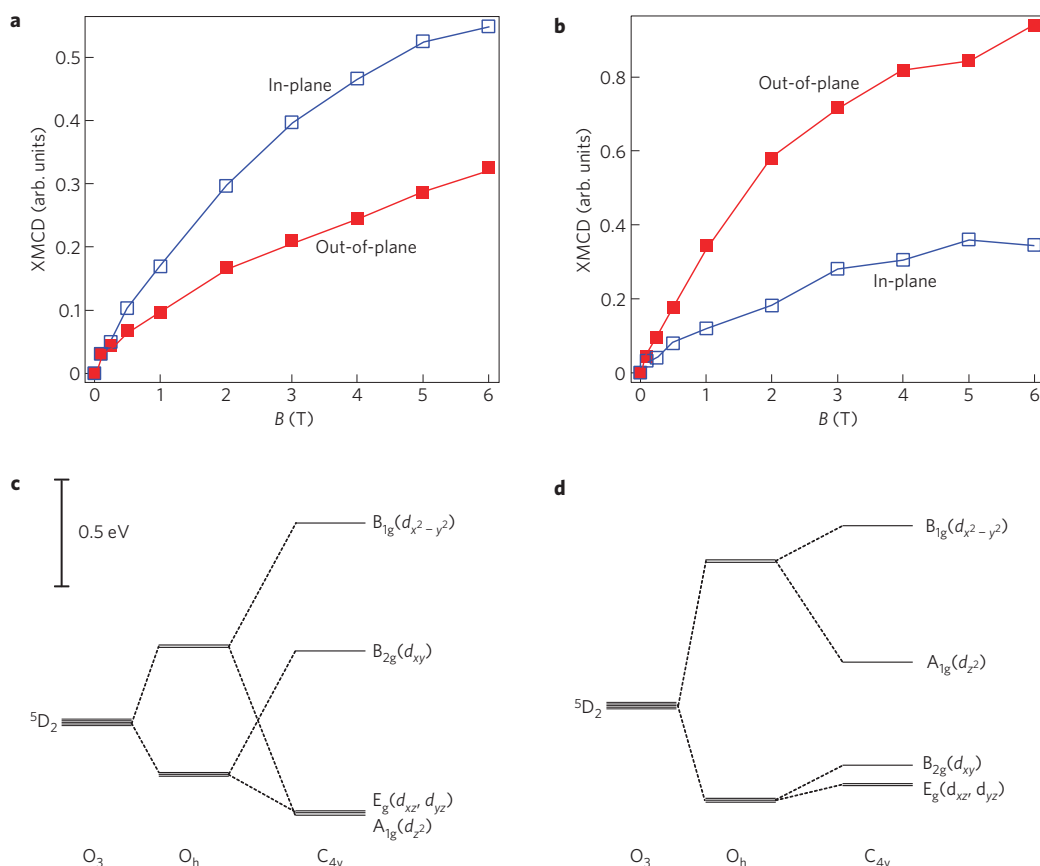


Figure 3 | Element-selective magnetization curves of the Fe centres and crystal-field diagrams. a, b, Fe(TPA)₄ (a) and O₂-Fe(TPA)₄ (b) magnetization measured at $T = 8$ K with the field applied out-of-plane ($\theta = 0^\circ$, filled symbols) and close to the in-plane direction ($\theta = 70^\circ$, open symbols). The data points represent the Fe XMCD intensity integrated over the L₃-edge and normalized by the corresponding L₃-integrated XAS intensity. **c, d**, Crystal-field diagram of Fe(TPA)₄ (c) and O₂-Fe(TPA)₄ (d) derived from the XAS multiplet simulations.

the E_g term in O₂-Fe(TPA)₄. The change of ground state has important consequences for the magnetic properties: before taking the spin-orbit perturbation on the crystal-field levels into account, the orbital angular momentum is quenched for an A_{1g} term. In C_{4v} symmetry, on the other hand, the E_g term is an orbitally degenerate doublet with non-zero orbital moment pointing along the principal symmetry direction. The tendency of O₂-Fe(TPA)₄ to magnetize out-of-plane, together with its stronger magnetic anisotropy compared with Fe(TPA)₄, can be traced back to its unperturbed crystal-field configuration and non-zero first-order orbital moment perpendicular to the surface plane. In Fe(TPA)₄, the orbital moment arises as a second-order perturbation effect as spin-orbit coupling admixes the nearly degenerate A_{1g} and E_g states²⁸. XMCD sum-rule measurements reflect the difference between the two compounds, showing that O₂-Fe(TPA)₄ has 30% higher orbital magnetic moment compared with Fe(TPA)₄, namely 0.55 ± 0.07 and $0.42 \pm 0.06 \mu_B$ at $T = 8$ K, when $B = 6$ T is applied out-of-plane and in-plane, that is, along the respective easy magnetization direction. Note that the orbital magnetic moment measured for Fe/Cu(100) is much smaller, $0.18 \pm 0.03 \mu_B$. A complete discussion of the sum-rule analysis is reported in Supplementary Information.

The ligand-field calculations yield zero-field splitting of about -3 and $+5$ meV for Fe(TPA)₄ and O₂-Fe(TPA)₄, respectively. However, we caution that these parameters may be overestimated by as much as a factor of two, as are the ligand-field predictions for the orbital moments, owing to covalency effects that are not treated in the ligand-field approach²⁸. Our data disclose an extra unusual effect for surface magnetic systems, namely the

strong anisotropy of the saturation magnetic moments of Fe. This effect is borne out both by the XMCD curves in Fig. 3 and the ligand-field calculations, which reveal a large and highly anisotropic orbital magnetization due to the predominant influence of the low-symmetry ligand field over the Fe-metal interaction, and confirmed by the different XMCD multiplet structure observed at $\theta = 70^\circ$ relative to 0° (see Supplementary Information, Fig. S2). Finally, we note that no sign of magnetic coupling was detected between the Fe centres. Future investigations may address this issue using different kinds of molecular ligand to adjust the Fe-Fe spacing and spin-dependent electron correlation.

The spin behaviour of individual atoms in purely metallic and molecular environments has been intensively studied in recent years, leading to the discovery of unusual magnetic^{1-4,12,17} and electron transport properties^{29,30}. The capability to fabricate 2D arrays of monodisperse spin centres with nanometre spacing, and to understand and control their magnetic properties at the interface with a metal substrate, constitutes a basic step towards the exploitation of single-spin phenomena in heterogeneous devices based on either a mono- or multilayer geometry.

Methods

Experiments were carried out at the ID08 beamline of the European Synchrotron Radiation Facility in Grenoble. Fe(TPA)₄ and O₂-Fe(TPA)₄ layers were prepared by sequential deposition of TPA and Fe on a clean Cu(100) surface and characterized *in situ* by STM and low-energy electron diffraction before the XAS measurements. Ultrahigh-vacuum conditions were maintained throughout the structural and XAS characterization measurements. For further details about the sample preparation, multiplet calculations and XMCD analysis, see Supplementary Information. The DFT calculations were carried out using the generalized gradient approximation as the exchange-correlation functional of the Kohn-Sham equations using the

Vienna *Ab-initio* Simulation Package code (<http://cms.mpi.univie.ac.at/vasp/>). The electronic wavefunctions were expanded in a plane-wave basis set, up to a cutoff energy of 37 Ryd, and the core–valence interaction was modelled with the projected augmented-wave method. Three substrate layers (first fully relaxed with adsorbate layer, second only laterally) together with almost 20 Å of vacuum between the two surfaces of the slab were used. A (2 × 2) grid of Monkhorst–Pack *k*-points in the first Brillouin zone was used to approximate the integration over the reciprocal space during the atomic relaxation, and a (4 × 4) grid was used for the analysis.

Received 17 July 2008; accepted 22 December 2008;
published online 1 February 2009

References

- Gambardella, P. *et al.* Giant magnetic anisotropy of single cobalt atoms and nanoparticles. *Science* **300**, 1130–1133 (2003).
- Meier, F., Zhou, L., Wiebe, J. & Wiesendanger, R. Revealing magnetic interactions from single-atom magnetization curves. *Science* **320**, 82–86 (2008).
- Heinrich, A. J., Gupta, J. A., Lutz, C. P. & Eigler, D. M. Single-atom spin-flip spectroscopy. *Science* **306**, 466–469 (2004).
- Hirjibehedin, C. F. *et al.* Large magnetic anisotropy of a single atomic spin embedded in a surface molecular network. *Science* **317**, 1199–1203 (2007).
- Eigler, D. M. & Schweitzer, E. K. Positioning single atoms with a scanning electron microscope. *Nature* **344**, 524–526 (1990).
- Nagaoka, T., Jamneala, T., Grobis, M. & Crommie, M. F. Temperature dependence of a single Kondo impurity. *Phys. Rev. Lett.* **88**, 077205 (2002).
- Wahl, P. *et al.* Kondo effect of molecular complexes at surfaces: Ligand control of the local spin coupling. *Phys. Rev. Lett.* **95**, 166601 (2005).
- Monso, S. *et al.* Crossover from in-plane to perpendicular anisotropy in Pt/CoFe/AlOx sandwiches as a function of Al oxidation: A very accurate control of the oxidation of tunnel barriers. *Appl. Phys. Lett.* **80**, 4157–4159 (2002).
- Hong, J., Wu, R. Q., Lindner, J., Kosubek, E. & Baberschke, K. Manipulation of spin reorientation transition by oxygen surfactant growth: A combined theoretical and experimental approach. *Phys. Rev. Lett.* **92**, 147202 (2004).
- Sander, D. *et al.* Reversible H-induced switching of the magnetic easy axis in Ni/Cu(001) thin films. *Phys. Rev. Lett.* **93**, 247203 (2004).
- Peterka, D., Enders, A., Haas, G. & Kern, K. Adsorbate and thermally induced spin reorientation transition in low-temperature-grown Fe/Cu(001). *Phys. Rev. B* **66**, 104411 (2002).
- Bogani, L. & Wernsdorfer, W. Molecular spintronics using single-molecule magnets. *Nature Mater.* **7**, 179–186 (2008).
- Naber, W. J. M., Faez, S. & van der Wiel, W. G. Organic spintronics. *J. Phys. D* **40**, R205–R228 (2007).
- Parkin, S. S. P. *et al.* Magnetically engineered spintronic sensors and memory. *Proc. IEEE* **91**, 661–680 (2003).
- Fukuzawa, H. *et al.* Specular spin-valve films with an FeCo nano-oxide layer by ion-assisted oxidation. *J. Appl. Phys.* **91**, 6684–6690 (2002).
- Scheybal, A. *et al.* Induced magnetic ordering in a molecular monolayer. *Chem. Phys. Lett.* **411**, 214–220 (2005).
- Wende, H. *et al.* Substrate-induced magnetic ordering and switching of iron porphyrin molecules. *Nature Mater.* **6**, 516–520 (2007).
- Atodiresei, N. *et al.* Controlling the magnetization direction in molecules via their oxidation state. *Phys. Rev. Lett.* **100**, 117207 (2008).
- Ruben, M., Rojo, J., Romero-Salguero, F. J., Uppadine, L. H. & Lehn, J.-M. Grid-type metal ion architectures: Functional metallosupramolecular arrays. *Angew. Chem. Int. Ed.* **43**, 3644–3662 (2004).
- Stepanow, S. *et al.* Steering molecular organization and host–guest interactions using two-dimensional nanoporous coordination systems. *Nature Mater.* **3**, 229–233 (2004).
- Semenov, A. *et al.* Controlled arrangement of supramolecular metal coordination arrays on surfaces. *Angew. Chem. Int. Ed.* **38**, 2547–2550 (1999).
- Barth, J. V., Costantini, G. & Kern, K. Engineering atomic and molecular nanostructures at surfaces. *Nature* **437**, 671–679 (2005).
- Lingenfelder, M. A. *et al.* Towards surface-supported supramolecular architectures: Tailored coordination assembly of 1,4-benzenedicarboxylate and Fe on Cu(100). *Chem. Eur. J.* **10**, 1913–1919 (2004).
- Stepanow, S., Lin, N. & Barth, J. V. Modular assembly of low-dimensional coordination architectures on metal surfaces. *J. Phys. Condens. Matter* **20**, 184002 (2008).
- de Groot, F. & Kotani, A. *Core Level Spectroscopy of Solids* (CRC Press, 2008).
- Gambardella, P. *et al.* Localized magnetic states of Fe, Co, and Ni impurities on alkali metal films. *Phys. Rev. Lett.* **88**, 047202 (2002).
- Hocking, R. K. *et al.* Fe L-edge X-ray absorption spectroscopy of low-spin heme relative to non-heme Fe complexes: Delocalization of Fe d-electrons into the porphyrin ligand. *J. Am. Chem. Soc.* **129**, 113–125 (2007).
- Figgis, B. N. & Hitchman, M. A. *Ligand Field Theory and Its Applications* (Wiley–VCH, 2000).
- Rocha, A. R. *et al.* Towards molecular spintronics. *Nature Mater.* **4**, 335–339 (2005).
- Timm, C. & Elste, F. Spin amplification, reading, and writing in transport through anisotropic magnetic molecules. *Phys. Rev. B* **73**, 235304 (2006).

Acknowledgements

We acknowledge the ESRF for provision of beam time. Partial financial support was received through the EUROCORES 05-SONS-FP-009 SANMAG project of the European Science Foundation. P.G. and S.S. acknowledge financial support from the Spanish Ministerio de Educación y Ciencia (SYNSPIN—MAT2007-62341).

Additional information

Supplementary Information accompanies this paper on www.nature.com/naturematerials. Reprints and permissions information is available online at <http://npg.nature.com/reprintsandpermissions>. Correspondence and requests for materials should be addressed to P.G.

Supplementary Information

Supramolecular control of the magnetic anisotropy in two-dimensional high-spin Fe arrays at a metal interface

Pietro Gambardella^{1,2,3}, Sebastian Stepanow^{1,4}, Alexandre Dmitriev^{4,5}, Jan Honolka⁴, Frank de Groot⁶, Magalí Lingenfelder⁴, Subhra Sen Gupta⁷, D.D. Sarma⁷, Peter Bencok⁸, Stefan Stanescu⁸, Sylvain Clair³, Stefan Pons³, Nian Lin⁴, Ari P. Seitsonen⁹, Harald Brune³, Johannes V. Barth¹⁰ and Klaus Kern^{3,4}

¹ *Centre d'Investigacions en Nanociència i Nanotecnologia (ICN-CSIC), UAB Campus, E-08193 Barcelona, Spain*

² *Institució Catalana de Recerca i Estudis Avançats (ICREA), E-08010 Barcelona, Spain*

³ *Institut de Physique des Nanostructures, Ecole Polytechnique Fédérale de Lausanne (EPFL), CH-1015 Lausanne, Switzerland*

⁴ *Max-Planck-Institut für Festkörperforschung, D-70569 Stuttgart, Germany*

⁵ *Department of Applied Physics, Chalmers University of Technology, 41296 Göteborg, Sweden*

⁶ *Department of Chemistry, Utrecht University, 3584 CA Utrecht, The Netherlands*

⁷ *Solid State and Structural Chemistry Unit, Indian Institute of Science, Bangalore 560 012, India*

⁸ *European Synchrotron Radiation Facility, BP 200, F-38043 Grenoble, France*

⁹ *Institut de Minéralogie et de Physique des Milieux Condensé, Université Pierre et Marie Curie, F-75252 Paris, France*

¹⁰ *Physik-Department E20, Technische Universität München, D-85748 Garching, Germany*

Sample preparation

Samples were prepared and characterized in-situ under ultra-high-vacuum conditions (UHV, base pressure 2×10^{-10} mbar). The single-crystal Cu(100) substrate was cleaned by sputtering (Ar⁺, 800 V) and annealing cycles up to 600 K until a sharp (100) low-energy electron diffraction (LEED) pattern was obtained; the presence of surface contaminants such as O, CO, and impurity metals other than Cu was below the detection threshold of x-ray absorption spectroscopy (XAS). To fabricate the two-dimensional metal-organic networks, a molecular precursor layer of 1,4-benzenedicarboxylic acid (terephthalic acid, TPA) was deposited at room temperature from a Knudsen cell heated to 450 K. TPA spontaneously forms a close-packed commensurate monolayer with a 3x3 unit cell, with all molecules lying flat parallel to the surface plane. Cu-induced deprotonation of the TPA carboxylic groups provides reactive carboxylate ligands¹. Self-assembly of supramolecular Fe(TPA)₄ complexes occurs upon deposition of Fe from an electron beam evaporator source on the molecular precursor layer, and annealing to 420 K^{2,3,4}. The absolute TPA and Fe coverages were calibrated using a quartz microbalance and scanning tunneling microscopy (STM). The maximum yield of Fe(TPA)₄, estimated by STM as > 90%, is obtained by depositing one Fe atom every four TPA molecules, corresponding to 0.025 Fe monolayers (1 ML = 1×10^{15} atoms/cm²). Due to the strength of the metal-ligand interaction, Fe(TPA)₄ complexes are thermally stable up to 500 K. O₂-Fe(TPA)₄ spontaneously forms upon O₂ dosing (1×10^{-8} mbar) at room temperature. The oxygen exposure was 72 L (Langmuirs) for the image presented in Fig. 1 b, and 216 L for the samples investigated by XAS, corresponding to about 96% saturation of the Fe sites. Contrary to the related Fe₂(TPA)₂ compound on Cu(100), which breaks up as a result of O₂ exposure, no change of the supramolecular network structure was observed other than the local modification of the electronic density of states at the Fe sites evidenced by constant current STM images (Fig. 1b). For each sample, the quality and homogeneity of Fe(TPA)₄ and O₂-Fe(TPA)₄ networks was checked by LEED and STM by repeatedly probing different sample regions within a 2x2 mm² square; a representative STM image of Fe(TPA)₄ is shown in Fig. S1. Samples with incomplete Fe incorporation in the TPA layer, as well as excess Fe or TPA species were discarded as they yield readily observable phases with either a disordered or ordered 3x3 structure different from the 6x6 Fe(TPA)₄ pattern. Sample transfer from the STM preparation chamber to the 6 Tesla magnet used for the XAS measurements was performed in-situ maintaining UHV conditions throughout the experiment.

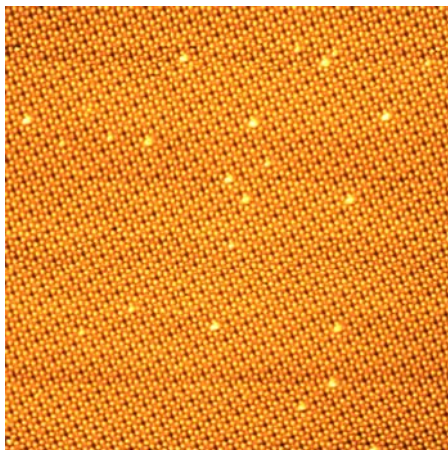


Figure S1: STM image of a supramolecular $\text{Fe}(\text{TPA})_4$ array self-assembled on $\text{Cu}(100)$, showing the periodicity of the $\text{Fe}(\text{TPA})_4$ pattern on an extended scale. Image size $520 \times 520 \text{ \AA}^2$.

XAS and XMCD measurements

The experiments were performed on beamline ID08 of the European Synchrotron Radiation Facility located in Grenoble, using the photon beam provided by an APPLE II undulator source with $99 \pm 1\%$ circular polarization rate. The energy resolution was set to about 200 meV using 20 μm entrance and exit slits for a dragon-type monochromator with 1200 lines/mm dispersive grating. The sample holder was tightly screwed at the bottom of a liquid helium flow cryostat and placed in a thermally-shielded environment between the two coils of a superconducting split magnet, which produced a variable field $\mathbf{B} = -6$ to 6 T collinear with the incident x-ray direction. The temperature at the sample position was calibrated using a Cernox[®] thermometer mounted on a standard sample holder. A differentially-pumped rotary feedthrough allowed for the rotation of the sample with respect to \mathbf{B} and the x-ray beam. XAS measurements were performed in the total electron yield (TEY) mode by measuring the drain current of the sample as a function of photon energy. The sample current was flux normalized by the photocurrent of a gold grid reference monitor placed between the last refocussing mirror and the sample itself. The beam spot size at the sample position was $0.1 \times 1 \text{ mm}^2$ FWHM.

Fe spectra: The data shown here were recorded over the Fe $L_{2,3}$ energy range for parallel (I^+) and antiparallel (I^-) alignment of the photon helicity with \mathbf{B} at $T = 8 \text{ K}$. For each set, we present averages of four scans taken at opposite field values in order to cancel out possible spurious effects due to the alignment of \mathbf{B} . X-ray magnetic circular dichroism (XMCD) spectra are

given by the difference $I^+ - I^-$; the angle θ between the surface normal and \mathbf{B} was varied in order to study the angular magnetization dependence. Figure S2a shows the XAS spectra of Fe/Cu(100), Fe(TPA)₄, and O₂-Fe(TPA)₄ prior to background subtraction. The Cu signal, shown at the bottom, provides the strongest XAS intensity in absolute terms, with the Fe edge jump representing about 2% of the TEY. Such background is nonmagnetic and has no influence on the XMCD, shown in Fig. S2b, but hampers the comparison between experimental data and theory; it has been subtracted from the data reported in Fig. 2 and Fig. S3.

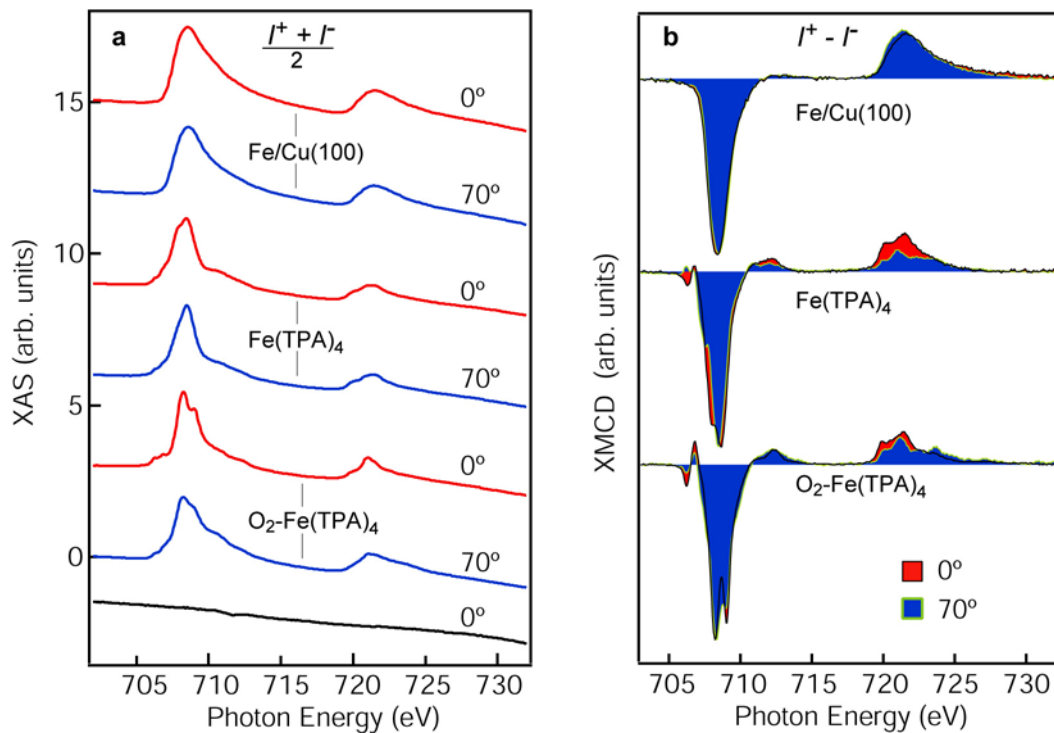


Figure S2: **a**, Top to bottom: x-ray absorption spectra of Fe/Cu(100), Fe(TPA)₄, O₂-Fe(TPA)₄, and Cu background measured at the Fe $L_{2,3}$ edge. **b**, Comparison of the XMCD spectral lineshape of the same compounds after normalization to the intensity minimum at the L_3 edge. Spectra were recorded at $T = 8$ K and $\mathbf{B} = 6$ T at normal ($\theta = 0^\circ$) and grazing incidence ($\theta = 70^\circ$).

It is well known that the $L_{2,3}$ edge spectra of transition-metals are composed by the sum of $2p \rightarrow 3d$ and $2p \rightarrow 4s$ transitions, the latter being one order of magnitude less-intense compared to the former⁵. The so-called $2p \rightarrow 4s$ continuum contribution is usually modeled as

a double arctan function with steps in correspondence of the $2p \rightarrow 3d$ resonance⁶, as shown by the thin solid line in Fig. S3, and subtracted from the total XAS in order to apply the XMCD sum rules^{6,7,8}. In ionic transition-metal compounds and molecules, however, it is found that the relative weight of the $2p \rightarrow 3d$ versus $2p \rightarrow 4s$ transitions increases compared to bulk metals near the excitation threshold due to d -electron localization, while the $4s$ threshold may shift up in energy⁹. The first effect is found here (Fig. S3), but a step-like contribution is still evident for $\text{Fe}(\text{TPA})_4$ and $\text{O}_2\text{-Fe}(\text{TPA})_4$ after background subtraction, suggesting that the Fe $4s$ states are still partially hybridized with Cu, in agreement with density-functional theory (DFT) calculations.

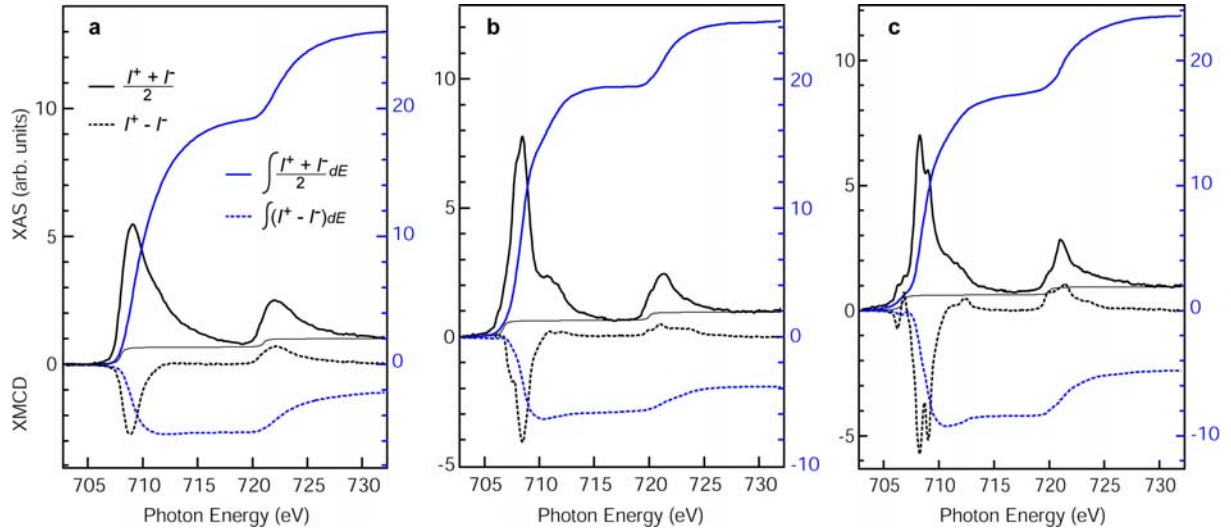


Figure S3: Integration of the XAS and XMCD spectra and sum rule analysis of **a**, 0.025 monolayers Fe/Cu(100) ($\theta = 0^\circ$); **b**, $\text{Fe}(\text{TPA})_4$ ($\theta = 70^\circ$); **c**, $\text{O}_2\text{-Fe}(\text{TPA})_4$ ($\theta = 0^\circ$).

O spectra: The data were recorded over the O K edge at $\theta = 0^\circ$ and 70° , using the same field and temperature as for Fe. No clear XMCD signal could be detected outside the noise level, even though the DFT calculations show the presence of an induced spin polarization localized at the O sites next to the Fe centers (Fig. 1d). This is not surprising given that the magnitude of the induced moment in the O p states is the order of $0.01 \mu_B$ and that the K -edge XMCD is sensitive to the $2p$ -projected orbital moment with a cross section about two orders of magnitude smaller compared to the $L_{2,3}$ thresholds. Further, there are only four O neighbors per Fe atom over a total of sixteen O atoms in $\text{Fe}(\text{TPA})_4$. The total XAS intensity ($I^+ + I^-$), however, contains information about the bonding of the O atoms. Due to the dipole selection

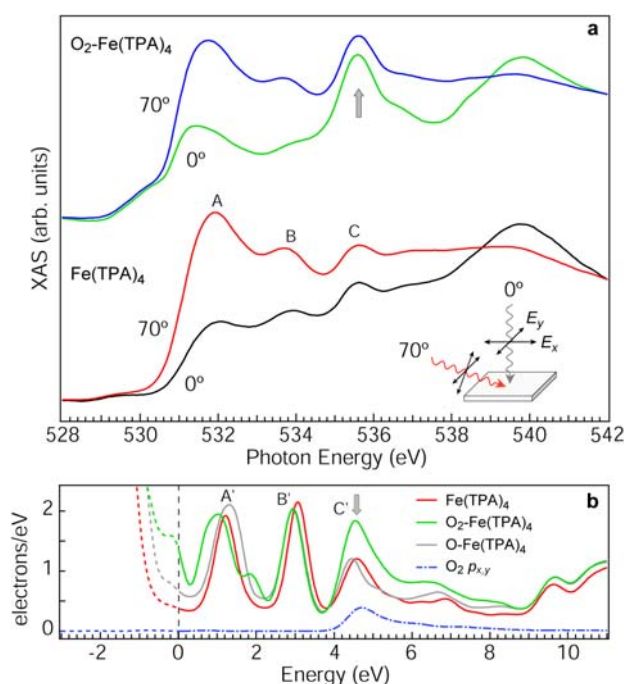


Figure S4: a, O K edge x-ray absorption spectra of Fe(TPA)_4 and $\text{O}_2\text{-Fe(TPA)}_4$; b, Calculated O-projected DOS of Fe(TPA)_4 , $\text{O}_2\text{-Fe(TPA)}_4$, and O-Fe(TPA)_4 obtained by summation over all O atoms in the unit cell (solid lines) and for the O_2 ligand only projected onto the $p_{x,y}$ orbital (dash-dotted line).

mechanism, a larger absorption intensity is expected when the electric field vector (\mathbf{E}) of the incident photon beam is aligned parallel to an empty orbital¹⁰. Figure S4 shows the $I^+ + I^-$ spectra of O in Fe(TPA)_4 and $\text{O}_2\text{-Fe(TPA)}_4$, which correspond to the sum of linearly polarized spectra with \mathbf{E} parallel and perpendicular to the incidence plane, together with the oxygen-projected density of states (DOS) calculated by density functional theory (DFT) calculations (see below). Owing to the small core-hole effects, K-edge spectra may be considered as a first-order approximation of the oxygen p -projected unoccupied DOS^{11,12}. Here, we find a one-to-one correspondence between the low-energy XAS peaks A, B, and C and the three most intense features in the oxygen unoccupied DOS indicated as A', B', and C' in Fig. S4. The analysis of the p -projected DOS reveals that such features arise from states with mainly p_z character involved in O-C antibonding π^* orbitals, whose XAS resonance intensity is expected to be large when probed at grazing incidence, as confirmed by the $\theta = 70^\circ$ spectra relative to $\theta = 0^\circ$. The angular dependence is consistent with the O K-edge spectra of deprotonated carboxylic groups in glycine adsorbed on Cu(110) ¹³. The spectra of $\text{O}_2\text{-Fe(TPA)}_4$ and

Fe(TPA)₄ are rather similar, which is expected based on the small relative change of O stoichiometry. The most prominent difference, however, is a net increase of the intensity of peak C (arrow in Fig. S4a), which is traced back to O₂ states with p_x and p_y character in the unoccupied DOS calculated for O₂ chemisorbed on top of the Fe(TPA)₄ metal center (Fig. S4b, dash-dotted line). The corresponding enhancement of peak C' in the DOS is found to be a characteristic feature of O₂ chemisorbed on top of the metal site in Fe(TPA)₄ with the molecular axis parallel to the surface plane, and is not reproduced by other molecular structures such as, e.g., atomically chemisorbed O at the Fe sites (labelled O-Fe(TPA)₄ in Fig. S4 b). In agreement with this interpretation, the intensity of peak C in the O₂-Fe(TPA)₄ spectra is found to be larger at $\theta = 0^\circ$ compared to $\theta = 70^\circ$. Note that the catalytic activity of the Fe sites can be tuned by the relative stoichiometry of Fe with respect to the TPA ligands; in particular, O₂ dissociation requires the presence of two Fe centers close to each other, as shown by a recent study of Fe-dimer carboxylate networks¹⁴.

Multiplet calculations

To interpret the XAS and XMCD spectra of Fe(TPA)₄ and O₂-Fe(TPA)₄ we used the theoretical simulation approach based on the atomic theory described by Cowan¹⁵, with the addition of crystal field interactions¹⁶, and the multiplet model implemented by Thole and coworkers^{17,18}. The atomic many-body Hamiltonian includes the on-site energies of the Fe $2p$ and $3d$ levels, full multiplet Coulomb interaction within the $3d$ shell and between the $2p$ and $3d$ manifolds, as well as spin-orbit coupling in each subshell. The Slater integrals calculated by Hartree-Fock theory were reduced to 80% of the free ion values to account for over-estimation of the electron-electron repulsion in solid and molecular compounds. The Fe environment was simulated using a crystal field (CF) potential with C_{4v} symmetry defined by the parameters $10Dq$, Ds , and Dt . Covalent mixing between the metal d -orbitals with the ligand valence p -orbitals was further taken into account by a charge-transfer model where two states, d^6 and $d^7\bar{L}$, are mixed by configuration interaction. The charge-transfer parameters Δ_i and Δ_f describe the separation between the d^6 and $d^7\bar{L}$ configurations in the initial and final state, respectively, and we allow for anisotropic hopping parameters for terms with unequal symmetry to account for their different covalent mixing. The effects of the substrate are not explicitly taken into account by this approach. This may be justified *a posteriori* by the very good agreement between simulated and measured spectra, which is indicative of the strong localization of the Fe d states. Moreover, we note that ab-initio one-electron schemes such as DFT usually employed to model surface systems do not reproduce correctly electron correlation effects in transition

metals, which are responsible for the sharp multiplet features observed in Fig. 2. The spectra are calculated from the sum of all dipole-allowed transitions between Fe $2p$ and $3d$ states, weighted by the appropriate Boltzmann factors to take into account finite temperature effects ($T = 8$ K). To reproduce the XMCD, a 6 T magnetic field was applied parallel to the C_{4v} high-symmetry axis, which corresponds to the XMCD spectra measured at $\theta = 0^\circ$ in Fig. 2. The XMCD spectra at $\theta = 70^\circ$ could not be simulated due to lowering of the symmetry beyond C_{4v} .

Table S1 reports the optimized CF parameters obtained after systematical analysis of the calculated vs. measured XAS and XMCD lineshape. The best agreement was found for a predominantly d^6 configuration with maximum 15% $d^7\bar{L}$ weight for both Fe(TPA) $_4$ and O $_2$ -Fe(TPA) $_4$. Within this configuration interaction range, the spectral shape is essentially governed by the relative position of the A_{1g} and E_g states, and can be equally well reproduced by the two sets of parameters reported below.

Table S1. Ligand-field parameters employed in the multiplet XAS calculations of Fe(TPA) $_4$ and O $_2$ -Fe(TPA) $_4$. The pure d^6 and mixed $d^6 + d^7\bar{L}$ configurations fit the spectra equally well when the ligand field parameters are adjusted as shown, and are therefore both reported here. 10Dq, Ds, and Dt are the usual crystal field parameters for C_{4v} symmetry. Δ_i and Δ_f represent the energy difference between the d^n and $d^{n+1}\bar{L}$ configurations in the initial and final state, respectively. Units are eV. The mixing parameters describe the relative weight of hopping between B_{1g} , A_{1g} , B_{2g} , and E_g terms.

	Configuration	10Dq	Ds	Dt	Δ_i	Δ_f	mixing
Fe(TPA) $_4$	d^6	0.58	0.29	0.03	-	-	-
Fe(TPA) $_4$	$0.86 d^6 + 0.14 d^7\bar{L}$	0.63	0.26	0.03	6	5	2 1.5 2 1.8
O $_2$ -Fe(TPA) $_4$	d^6	1.03	0.10	0.04	-	-	-
O $_2$ -Fe(TPA) $_4$	$0.85 d^6 + 0.15 d^7\bar{L}$	0.79	0.11	0.05	4	3	2 2 1 1

Ligand field parameters and Fe-projected DOS

The crystal field splitting diagrams for Fe(TPA) $_4$ and O $_2$ -Fe(TPA) $_4$ derived from the parameters in Table S1 are close to square planar and square pyramidal, respectively, as may be expected based on simple geometry considerations. There are, however, several comments

to be made, first with respect to the magnitude of the ligand field parameters and, second, to the influence of the substrate and the comparison with band structure DFT calculations.

Based on XAS simulations, 10Dq values of divalent Fe in bulk octahedral oxides such as FeO and FeAl₂O₄ are usually assumed to be close to 0.7 eV^{13,19,20}, while 0.9 eV has been reported for oxygen-bridged dinuclear iron molecular complexes²¹. When comparing these parameters with those derived from UV-visible spectroscopy, one must notice that the XAS 10Dq values are actually final state values, since the x-ray absorption lineshape depends mostly on final state effects, contrary to the integrated intensity, which is related to ground state properties. Due to the presence of the core-hole and the contraction of the 3d states, 10Dq might result up to 25% smaller in XAS compared to UV-visible spectroscopy²². Perhaps more importantly, we shall stress that 10Dq in our case does not represent the actual splitting between E_g and T_{2g} states: the energy of states having different symmetry is strongly affected by tetragonal distortion and eventually bears little resemblance with a cubic crystal field diagram. The strength of the tetragonal distortion given by D_s and D_t relative to 10Dq is found to decrease substantially upon O₂ adsorption, consistently with the formation of axial Fe-O₂ bonds and the weakening of lateral Fe-O interactions evidenced by DFT.

As mentioned before, the Fe-substrate interaction cannot be explicitly modelled using the ligand field approach. From a theoretical point of view, the competition and coexistence of metallic and molecular bonds with strong intra-atomic correlation interactions represents a formidable challenge, as there is no simple way of relating single-particle wavefunctions used in the description of itinerant systems with many-electron atomic states. Nonetheless, this interplay constitutes one of the most important issues in the study of metal-organic complexes on metals, since it drives their assembly and structure as well as determines their magnetic and electric transport properties. Local magnetic properties are most sensitive to electron correlation effects and are therefore best treated using an effective ligand field approach. DFT calculations provide a complementary framework that exemplifies the complexity of such systems. Figure S5 shows the calculated Fe 3d-projected DOS of Fe(TPA)₄ and O₂-Fe(TPA)₄. It can be easily recognized that the splitting pattern of the one-electron Fe *d* orbitals is indeed very far from octahedral, as expected based on the ligand field simulations. A direct comparison between the 3d DOS features and the crystal field diagrams of Fig. 3c,d is not appropriate, as the energy level spacings in the crystal field approach result from a many-electron calculation including both spin and orbital correlation. Moreover, the definition of crystal field parameters starting from ab-initio methods is not unique and turns out to be

particularly difficult for systems where the bandwidth is comparable or larger than the crystal field and a clear e_g-t_{2g} separation does not exist²³, as is the case here. Nonetheless, we observe that the most prominent high-energy DOS feature has $d_{x^2-y^2}$ symmetry for $\text{Fe}(\text{TPA})_4$, in agreement with the ligand field results. The energy separation between $d_{x^2-y^2}$ and d_{z^2} features is about 1.9 and 1.0 eV for majority and minority electrons, respectively, i.e., on average slightly larger than the separation between B_{1g} and A_{1g} states (1.3 eV) obtained from the ligand field simulations. Due to the square planar symmetry, the d_{xz} and d_{yz} states are completely degenerate, while near degeneracy is found for the majority d_{z^2} and $d_{xz,yz}$ orbitals, as between the A_{1g} and E_g states in the crystal field diagram. When looking at the Fe 3d-DOS of $\text{O}_2\text{-Fe}(\text{TPA})_4$ one observes that the higher-lying orbital has d_{xz} character, as the orientation of the O_2 molecular axis is parallel to x in the DFT calculations. However, for symmetry reasons the configuration with O_2 parallel to y is degenerate with O_2 parallel to x , so that d_{xz} and d_{yz} are experimentally indistinguishable and the $d_{x^2-y^2}$ orbital turns out to be the most energetically unfavoured. Due to O_2 adsorption, the splitting between states with $d_{x^2-y^2}$ and d_{z^2} symmetry is considerably reduced, while prominent d_{z^2} features move up in energy, as expected based on crystal field arguments.

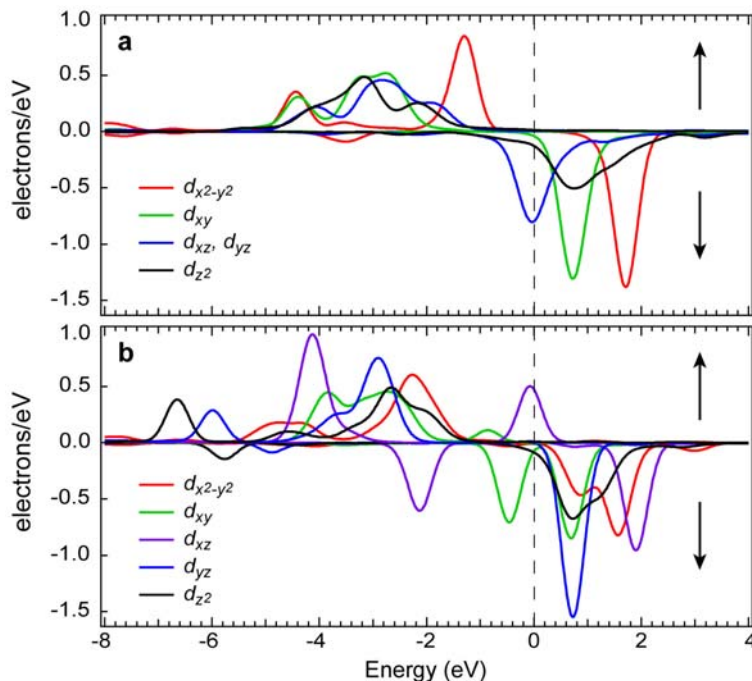


Figure S5: Spin-resolved Fe 3d-projected DOS of a, $\text{Fe}(\text{TPA})_4$ and b, $\text{O}_2\text{-Fe}(\text{TPA})_4$ as calculated by DFT and broadened by convolution with a Gaussian function of 0.5 eV FWHM.

DFT charge analysis

The electronic population of Fe, O, and Cu atoms was estimated using the Bader charge analysis method²⁴. As reported in Table S2, the total number of Fe valence electrons (including states with $3d$, $4s$, and $4p$ character) is 6.67 and 6.33 in $\text{Fe}(\text{TPA})_4$ and $\text{O}_2\text{-Fe}(\text{TPA})_4$, respectively. The O_2 molecule chemisorbed on Fe is negatively charged with 0.80 excess electrons. Interestingly, the majority of the extra electrons supplied to O_2 is found to originate from the metallic substrate, which acts as a charge reservoir for the $\text{Fe}(\text{TPA})_4$ complexes. We find that a depletion of 0.13 electrons per each of the four Cu nearest neighbors of Fe occurs upon O_2 adsorption. The remaining negative charge localized on O_2 is assigned to Fe $4sp$ electrons.

Bader's analysis is based on the integration of the total electron density within a partition of the atomic volume defined by "zero flux" surfaces. Alternative charge analysis techniques based on projection operators are discussed, e.g., in Ref. 25; one must note, however, that there is neither a unique nor an exact way of apportioning the electron density to a given atom in a solid or molecule. By relying on a spherical partition scheme defined by the

Table S2: Total number of valence electrons per atom obtained using the Bader analysis (Fe, Cu, O) and integrating the Fe 3d-PDOS (Fe 3d) as calculated by DFT.

$\text{Fe}(\text{TPA})_4$			
	↑	↓	Total
Fe	-	-	6.67
Fe $3d$	4.53	1.09	5.62
Cu	-	-	10.96
$\text{O}_2\text{-Fe}(\text{TPA})_4$			
Fe	-	-	6.33
Fe $3d$	4.56	1.10	5.66
Cu	-	-	10.83
O	-	-	6.40

extension of the projected augmented wave (PAW) potential, it is possible to separately compute the population of the Fe 3*d* states by integrating the 3*d*-projected DOS up to the Fermi level. This method tends to underestimate the actual 3*d* occupation since the interstitial charge is not taken into account correctly. Despite this, the integration of the Fe 3*d*-DOS up to the Fermi level gives 5.62 and 5.67 electrons for Fe(TPA)₄ and O₂-Fe(TPA)₄, respectively, which is compatible with the 3*d*⁶ configuration obtained in the ligand field simulations. Moreover, the small relative change of the 3*d* population between Fe(TPA)₄ and O₂-Fe(TPA)₄ further supports the stability of such a configuration with respect to O₂ chemisorption evidenced by the simulations. The difference between majority and minority 3*d* electrons may also serve to estimate the saturation spin magnetic moment of Fe, whose determination is not straightforward using the XMCD sum rules (see below). According to Table S2, we find 3.44 μ_B for Fe(TPA)₄ and a slightly larger value, 3.46 μ_B, for O₂-Fe(TPA)₄.

XMCD sum rule analysis and angular dependent magnetization curves

The spin and orbital sum rules are given below^{7,8}:

$$2\langle S_z \rangle + 7\langle T_z \rangle = \frac{9\int_{L_3} (I^+ - I^-) dE - 6\int_{L_3+L_2} (I^+ - I^-) dE}{\int_{L_3+L_2} (I^+ + I^- + I^0) dE} n_h, \quad (1)$$

$$\langle L_z \rangle = 2 \frac{\int_{L_3+L_2} (I^+ - I^-) dE}{\int_{L_3+L_2} (I^+ + I^- + I^0) dE} n_h, \quad (2)$$

where $\langle S_z \rangle$, $\langle L_z \rangle$, and $\langle T_z \rangle$ represent the expectation values of the spin, orbital, and spin dipolar moments of the 3*d* shell, respectively, with *z* indicating the incidence direction of the circularly-polarized x-ray beam. The terms in the denominator contain the integrated isotropic intensity $I^{iso} = I^+ + I^- + I^0$, which is a temperature- and field-independent constant proportional to the number of unoccupied *d*-states of the element under investigation. Here, I^0 stands for the XAS component measured with electric field vector parallel to the magnetization direction, *z*, a geometry which is usually not accessible in a single-magnet XMCD measuring setup. In metal systems, this term is therefore approximated with good accuracy by the average $I^0 = (I^+ + I^-)/2$ ⁶. Such an equivalency, however, is questionable for narrow-band and localized compounds^{26,27}. We estimate that, using $I^{iso} = 3/2 (I^+ + I^-)$ to calculate the sum rule-derived

magnetic moments for $\text{Fe}(\text{TPA})_4$ and $\text{O}_2\text{-Fe}(\text{TPA})_4$, as reported in Table S2, may introduce a relative error up to 12 %. The partial overlap of the L_2 and L_3 XMCD intensity introduces an additional uncertainty in the determination of $2\langle S_z \rangle + 7\langle T_z \rangle$ (Eq. 1); for an extensive discussion on the accuracy of the spin sum rule the reader is referred to de Groot and Kotani¹⁸. The integrated XAS and XMCD spectra used in the analysis are shown in Fig. S3. Note that only the easy axis sum rules moments approach saturation at $\mathbf{B} = 6$ T and $T = 8$ K. The Fe/Cu(100) magnetic moments are found to be in agreement with previous XMCD studies²⁸.

The angular dependence of the magnetization was probed by varying the incidence direction of the x-ray beam with respect to the sample. As the absolute TEY varies with θ , owing to the different x-ray probing depth at different incidence angles, the comparison of the angular-dependent XMCD intensity requires a self-consistent normalization procedure. This is achieved by normalizing the XMCD signal by the absorption $I^+ + I^-$. The curves in Fig. 3 report the XAS-normalized XMCD intensity integrated over the L_3 edge. According to Eqs. (1) and (2), this signal represents the quantity $2\langle S_z \rangle + 3\langle L_z \rangle + 7\langle T_z \rangle$, which is proportional to the spin magnetization $2\langle S_z \rangle$ at any given value of the applied field. An important results of our ligand-field model, however, is that $\langle L_z \rangle$ and $\langle T_z \rangle$ are strongly anisotropic at saturation. The anisotropy of $\langle T_z \rangle$ is calculated to oppose [follow] that of $\langle L_z \rangle$ for $\text{Fe}(\text{TPA})_4$ [$\text{O}_2\text{-Fe}(\text{TPA})_4$]. In neither case, however, the magnitude of the $7\langle T_z \rangle$ term, estimated to be smaller than $0.7 \mu_B$ in the present experimental conditions, affects the conclusions of this paper. The angular-dependent XMCD curves reflect both the magnetic anisotropy of the Fe ions as well as the tendency to saturate at different magnetic moment values. In bulk metals such an effect is present, but practically negligible. For Fe atoms in square-planar complexes, the low-symmetry molecular environment and unquenched orbital magnetization concur to make it substantial.

Table S3. Sum-rule derived magnetic moments from the XMCD spectra measured at $T = 8$ K, $B = 6$ T. Number of holes $n_h = 4$ for $\text{Fe}(\text{TPA})_4$ and $\text{O}_2\text{-Fe}(\text{TPA})_4$, 3.4 for $\text{Fe}/\text{Cu}(100)$. Magnetic moment values are given in μ_B/atom .

	$2\langle S_z \rangle + 7\langle T_z \rangle$	$\langle L_z \rangle$	$\frac{\langle L_z \rangle}{2\langle S_z \rangle + 7\langle T_z \rangle}$
$\text{Fe}(\text{TPA})_4 \theta = 0^\circ$	1.17	0.22	0.19
$\text{Fe}(\text{TPA})_4 \theta = 70^\circ$	1.56	0.42	0.27
$\text{O}_2\text{-Fe}(\text{TPA})_4 \theta = 0^\circ$	2.58	0.55	0.21
$\text{O}_2\text{-Fe}(\text{TPA})_4 \theta = 70^\circ$	0.90	0.25	0.28
$\text{Fe}/\text{Cu}(100) \theta = 0^\circ$	1.53	0.18	0.12
$\text{Fe}/\text{Cu}(100) \theta = 70^\circ$	1.33	0.14	0.11

References

¹ Stepanow, S., Strunskus, T., Lingenfelder, M., Dmitriev, A., Spillmann, H., Lin, N., Barth, J. V., Wöll, Ch. & Kern, K. Deprotonation-Driven Phase Transformations in Terephthalic Acid Self-Assembly on $\text{Cu}(100)$. *J. Phys. Chem. B* **108**, 19392-19397 (2004).

² Lingenfelder, M. A., Spillmann, H., Dmitriev, A., Stepanow, S., Lin, N., Barth, J. V. & Kern, K. Towards Surface-Supported Supramolecular Architectures: Tailored Coordination Assembly of 1,4-Benzenedicarboxylate and Fe on $\text{Cu}(100)$. *Chem. Eur. J.* **10**, 1913 – 1919 (2004).

³ Barth, J. V., Costantini, G., & Kern, K. Engineering atomic and molecular nanostructures at surfaces. *Nature* **437**, 671-679 (2005).

⁴ Stepanow, S., Lin, N. & Barth, J. V. Modular assembly of low-dimensional coordination architectures on metal surfaces. *J. Phys. Condens. Matter* **20**, 184002 (2008).

⁵ Yeh, J. J. & Lindau, I. Subshell photoionization cross sections. *At. Data Nucl. Data Tables* **32**, 1-155 (1985).

-
- ⁶ Chen, T.C., Idzerda, Y. U., Lin, H.-J., Smith, N. V., Meigs, G., Chaban, E., Ho, G. H., Pellegrin, E. & Sette, F. Experimental Confirmation of the XMCD Sum Rules for Iron and Cobalt. *Phys. Rev. Lett.* **75**, 152-155 (1995).
- ⁷ Thole, B.T., Carra, P., Sette, F. & van der Laan, G. X-ray circular dichroism as a probe of orbital magnetisation. *Phys. Rev. Lett.* **68**, 1943-1946 (1992).
- ⁸ Carra, P., Thole, B. T., Altarelli, M. & Wang, X. X-ray circular dichroism and local magnetic fields. *Phys. Rev. Lett.* **70**, 694-697 (1993).
- ⁹ van der Laan, G., Zaanen, J., Sawatzky, G. A., Karnatak, R. & Esteve, J.-M. Comparison of x-ray absorption with x-ray photoemission of nickel dihalides and NiO. *Phys. Rev. B* **33**, 4253 - 4263 (1986).
- ¹⁰ Stöhr, J. & Outka, D. A. Determination of molecular orientations on surfaces from the angular dependence of near-edge x-ray absorption fine structure spectra. *Phys. Rev. B* **36**, 7891 - 7905 (1987).
- ¹¹ De Groot, F., Grioni, M., Fuggle, J. C., Ghijsen, J., Sawatzky, G. A. & Petersen, H. Oxygen 1s x-ray-absorption edges of transition-metal oxides. *Phys. Rev. B* **40**, 5715 - 5723 (1989).
- ¹² van Elp, J. & Tanaka, A. Threshold electronic structure at the oxygen K edge of 3d-transition-metal oxides: a configuration interaction approach. *Phys. Rev. B* **60**, 5331 - 5339 (1999).
- ¹³ Nyberg, N., Hasselström, J., Karis, O., Wassdahl, N., Weinelt, M., Nilsson, A. & Pettersson, L. G. M. The electronic structure and surface chemistry of glycine adsorbed on Cu(110). *J. Chem. Phys.* **112**, 5420 (2000).
- ¹⁴ Fabris, S., Lin, N., Stepanow, S., Baroni, S. & Kern, K. Concerted catalytic action of di-iron centers dissociates O₂: modelling non-heme enzymes with metal-organic networks, to be published.

-
- ¹⁵ Cowan, R. D. *The Theory of Atomic Structure and Spectra*. (University of California Press, Berkely, 1981).
- ¹⁶ Butler, P. H. *Point Group Symmetry Applications: methods and Tables*. (Plenum Press, New York, 1981).
- ¹⁷ Thole, B. T., Cowan, R. D., Sawatzky, G. A., Fink, J. & Fuggle J.C. New probe for the ground-state electronic structure of narrow-band and impurity systems. *Phys. Rev. B* **31**, 6856 - 6858 (1985).
- ¹⁸ de Groot, F. & Kotani, A. *Core Level Spectroscopy of Solids*. (CRC Press, Boca Raton, 2008).
- ¹⁹ Crocombette, J. P., Pollak, M., Jollet, F., Thromat, N. & Gautier-Soyer, M. X-ray absorption at the Fe L_{2,3} threshold in iron oxides. *Phys. Rev. B* **52**, 3143 -3150 (1995).
- ²⁰ de Groot, F., Glatzel, P., Bergmann, U., van Aken, P., Barrea, R.A., Klemme, S., Havecker, M., Knop-Gericke, A., Heijboer, W.M. & Weckhuysen, B.M. 1s_{2p} Resonant inelastic x-ray scattering of iron oxides. *J. Phys. Chem. B* **109**, 20751 (2005).
- ²¹ Peng, G., van Elp, J., Jang, H., Que, L., Armstrong, W.H. & Cramer, S. P. L-edge x-ray absorption and x-ray magnetic circular dichroism of oxygen-bridged dinuclear iron complexes. *J. Am. Chem. Soc.* **117**, 2515-2519 (1995).
- ²² Cramer, S.P., de Groot, F.M.F., Ma, Y., Chen, C.T., Sette, F., Kipke, C.A., Eichhorn, D.M., Chan, M.K., Armstrong, W.H., Libby, E., Christou, G., Brooker, S., McKee, V., Mullins, O.C. & Fuggle, J.C. Ligand field strengths and oxidation states from manganese L-edge spectroscopy. *J. Am. Chem. Soc.* **113**, 7937-7940 (1991).
- ²³ Streltsov, S. V., Mylnikova, A. S., Shorikov, A. O., Pchelkina, Z. V., Khomskii, D. I. & Anisimov, V. I. Crystal-field splitting for low symmetry systems in ab initio calculations. *Phys. Rev. B* **71**, 245114 (2005).

²⁴ Bader, R.F.W. *Atoms in Molecules - A quantum theory*, Oxford University Press, New York, (1990).

²⁵ Clark, A. E., Davidson E., R. Population analyses that utilize projection operators. *Int. J. Quantum Chem.* **93**, 384 – 394 (2003).

²⁶ Van der Laan, G. & Thole, B.T. Strong magnetic x-ray dichroism in 2p absorption spectra of 3d transition-metal ions. *Phys. Rev. B* **43**, 13401 - 13411 (1991).

²⁷ Wu, R., Wang, D. & Freeman, A. J. First principles investigation of the validity and range of applicability of the x-ray magnetic circular dichroism sum rule. *Phys. Rev. Lett.* **71**, 3581 - 3584 (1993).

²⁸ Ohresser, P., Ghiringhelli, G., Tjernberg, O., Brookes N. B. & Finazzi, M. Magnetism of nanostructures studied by x-ray magnetic circular dichroism: Fe on Cu(111). *Phys. Rev. B* **62**, 5803 - 5809 (2000).